基于pNJL模型的三维QCD相图

刘鹿蒙　　徐骏　　彭光雄

Three-dimensional QCD Phase Diagram in the pNJL Model

LIU Lumeng, XU Jun, PENG Guangxiong

您可能感兴趣的其他文章

Articles you may be interested in

改进的PNJL模型下QCD的相图

QCD Phase Diagram in the Improved PNJL Model

原子核物理评论. 2017, 34(3): 575–579　https://doi.org/10.11804/NuclPhysRev.34.03.575

PNJL模型下手征相变的临界指数

Critical Exponents of the Chiral Phase Transition in the PNJL Model

原子核物理评论. 2020, 37(3): 705–712　https://doi.org/10.11804/NuclPhysRev.37.2019CNPC23

基于代数重建算法的高能电子三维成像研究

Study on Three−dimensional High Energy Electron Radiography Based on Algebraic Reconstruction Algorithm

原子核物理评论. 2021, 38(1): 73–79　https://doi.org/10.11804/NuclPhysRev.38.2020041

有限温下三维QED中费米速度对费米子手征凝聚的影响（英文）

Effect of Fermion Velocity on Fermion Chiral Condensate in QED_3 at Finite Temperature

原子核物理评论. 2017, 34(1): 16–19　https://doi.org/10.11804/NuclPhysRev.34.01.016

利用格点量子色动力学研究手征平滑过渡温度和手征相变温度

Chiral Crossover and Chiral Phase Transition Temperatures from Lattice QCD

原子核物理评论. 2020, 37(3): 674–678　https://doi.org/10.11804/NuclPhysRev.37.2019CNPC65

格点QCD组态产生研究

Generate Configurations for Lattice QCD Study

原子核物理评论. 2021, 38(2): 129–135　https://doi.org/10.11804/NuclPhysRev.38.2021022

Three-dimensional QCD Phase Diagram in the pNJL Model

LIU Lumeng[1], XU Jun[2,3,4,†], PENG Guangxiong[5]

(1. School of Physical Sciences, University of Chinese Academy of Sciences, Beijing 100049, China;

2. School of Physics Science and Engineering, Tongji University, Shanghai 200092, China;

3. Shanghai Advanced Research Institute, Chinese Academy of Sciences, Shanghai 201210, China;

4. Shanghai Institute of Applied Physics, Chinese Academy of Sciences, Shanghai 201800, China;

5. School of Nuclear Science and Technology, University of Chinese Academy of Sciences, Beijing 100049, China)

Abstract: Based on the three-flavor Polyakov-looped Nambu−Jona-Lasinio(pNJL) model, we have studied the structure of the three-dimensional QCD phase diagram with respect to the temperature, the baryon chemical potential, and the isospin chemical potential, by investigating the interplay among the chiral quark condensate, the pion condensate, and the Polyakov loop. While the pNJL model leads to qualitatively similar structure of the normal quark phase, the pion superfluid phase, and the Sarma phase as well as their phase boundaries, when compared to the NJL model, the inclusion of the Polyakov loop enlarges considerably the areas of the pion superfluid phase and the Sarma phase, and leads to critical end points at higher temperatures. With the contribution of the gluon dynamics effectively included, the present study is expected to give a more reliable prediction of the three-dimensional QCD phase diagram compared to that in the NJL model.

Key words: Nambu-Jona-Lasinio; QCD phase diagram; pion condensate

0 Introduction

Exploring the phase diagram of the quantum chromodynamics(QCD) has been a main task in high-energy nuclear physics over the past few decades. Although the lattice QCD (LQCD) calculations favor a smooth crossover from the hadronic phase to the partonic phase at high temperatures and small baryon chemical potentials[1−3], they suffer from the sign problem[4−6] at large baryon chemical potentials, where our knowledge on the QCD phase diagram mostly relies on experimental data from heavy-ion collisions, such as those performed at RHIC-BES[7−9], FAIR-CBM[10−11], GSI-HADES[12], CERN-NA61/SHINE[13−15], NICA/MPD[16], J-PARC-HI[17], and HIAF[18], as well as theoretical studies based on effective QCD models. The latter includes the NJL model[19−22], the Dyson-Schwinger (DS) equation approach[23−24], the functional renormalization group (FRG) method[25−26], and the quark-meson coupling model[27−29], *etc*. Besides the baryon chemical potential and the temperature, our knowledge on the QCD phase diagram can be extended to other degrees of freedom, *e.g.*, the isospin[30]. If the isospin chemical potential

exceeds the mass of a pion, pions can be produced out of the vacuum, and the resulting pion condensate may dominate the QCD phase structure at large isospin chemical potentials[31−46].

In the previous study, we have obtained the QCD phase diagram at finite temperatures, baryon chemical potentials, and isospin chemical potentials in the three-flavor NJL model[31]. Typically, we have fitted the coupling constants of the scalar-isovector and vector-isovector interactions by reproducing the physical pion mass and the isospin density from LQCD calculations in baryon-free quark matter, and then extrapolated the calculations to finite baryon chemical potentials. While the NJL model has the advantage of describing chiral phase transitions, it is well-known that this model lacks gluon dynamics and is unable to describe the deconfinement phase transition. For this reason, it gives a lower temperature of the QCD critical end point (CEP), compared to that obtained from the DS equation approach and the FRG method. To overcome this drawback, one needs to introduce the Polyakov loop into the NJL model[21, 47−48], leading to the so-called pNJL model. The Polyakov loop $\Phi(\bar{\Phi})$ is related to the excess free energy

for a static quark (anti-quark) in a hot gluon medium[49], and thus serves as an order parameter for the deconfinement phase transition which is characterized by the spontaneous breaking of the $Z(N_c)$ center symmetry of QCD. The exploration of the three-dimensional QCD phase diagram based on the pNJL model is helpful for understanding the interplay among different order parameters, e.g., the chiral condensate, the pion condensate, and the Polyakov loop, and mapping out the resulting detailed phase structures.

1 Theoretical framework

We start from the following Lagrangian density of the three-flavor pNJL model[50−52]

$$\mathcal{L}_{\text{pNJL}} = \bar{\psi}\left(i\gamma^\mu D_\mu + \hat{\mu}\gamma^0 - \hat{m}\right)\psi + \mathcal{L}_{\text{S}} + \mathcal{L}_{\text{V}} + \mathcal{L}_{\text{KMT}} + \mathcal{L}_{\text{IS}} + \mathcal{L}_{\text{IV}} - \mathcal{U}\left(\Phi, \bar{\Phi}, T\right), \quad (1)$$

where

$$\mathcal{L}_{\text{S}} = \frac{G_{\text{S}}}{2}\sum_{a=0}^{8}\left[\left(\bar{\psi}\lambda^a\psi\right)^2 + \left(\bar{\psi}i\gamma^5\lambda^a\psi\right)^2\right], \quad (2)$$

$$\mathcal{L}_{\text{V}} = -\frac{G_{\text{V}}}{2}\sum_{a=0}^{8}\left[\left(\bar{\psi}\gamma^\mu\lambda^a\psi\right)^2 + \left(\bar{\psi}\gamma^5\gamma^\mu\lambda^a\psi\right)^2\right], \quad (3)$$

$$\mathcal{L}_{\text{KMT}} = -K\left[\det\bar{\psi}\left(1+\gamma^5\right)\psi + \det\bar{\psi}\left(1-\gamma^5\right)\psi\right], \quad (4)$$

$$\mathcal{L}_{\text{IS}} = G_{\text{IS}}\sum_{a=1}^{3}\left[\left(\bar{\psi}\lambda^a\psi\right)^2 + \left(\bar{\psi}i\gamma^5\lambda^a\psi\right)^2\right], \quad (5)$$

$$\mathcal{L}_{\text{IV}} = -G_{\text{IV}}\sum_{a=1}^{3}\left[\left(\bar{\psi}\gamma^\mu\lambda^a\psi\right)^2 + \left(\bar{\psi}\gamma^5\gamma^\mu\lambda^a\psi\right)^2\right], \quad (6)$$

are the scalar-isoscalar term, the vector-isoscalar term, the Kobayashi-Maskawa-t'Hooft (KMT) term, the scalar-isovector term, and the vector-isovector term, respectively. In the above, $\psi = (u, d, s)^T$ represents the three-flavor quark fields with each flavor containing quark fields of three colors; $\hat{\mu} = \text{diag}(\mu_u, \mu_d, \mu_s)$ and $\hat{m} = \text{diag}(m_u, m_d, m_s)$ are the matrices of the chemical potential and the current quark mass for u, d, and s quarks; $D_\mu = \partial_\mu - iA_\mu$ is the covariant derivative with $A_\mu = \delta_\mu^0 A_0$, where $A_0 = gA_0^a\lambda^a/2 = -iA_4$ is the non-Abelian SU(3) gauge field with the gauge coupling g conveniently absorbed in the definition of A_μ; λ^a ($a = 1, \cdots, 8$) are the Gell-Mann matrices in SU(3) flavor space with $\lambda^0 = \sqrt{2/3}\mathbb{1}_3$; G_{S} and G_{V} are respectively the scalar-isoscalar and the vector-isoscalar coupling constant; G_{IS} and G_{IV} are respectively the scalar-isovector and the vector-isovector coupling constants. Since the Gell-Mann matrices with $a = 1, 2, 3$ are identical to the Pauli matrices

in u and d space, the isovector couplings break the SU(3) symmetry while keeping the isospin symmetry. K denotes the strength of the six-point KMT interaction[53] that breaks the axial $U(1)_{\text{A}}$ symmetry, where 'det' denotes the determinant in flavor space. In the present study, we employ the parameters $m_u = m_d = 3.6$ MeV, $m_s = 87$ MeV, $G_{\text{S}}\Lambda^2 = 3.6$, $K\Lambda^5 = 8.9$, and the cutoff value in the momentum integral $\Lambda = 750$ MeV/c given in Refs. [19, 54−55]. In our previous study[31], $G_{\text{IS}} = -0.002G_{\text{S}}$ and $G_{\text{IV}} = 0.25G_{\text{S}}$ are determined by fitting the physical pion mass $m_\pi \approx 140.9$ MeV and the reduced isospin density from LQCD calculations at zero temperature[56], at which the pNJL model reduces to the NJL model. We set $G_{\text{V}} = 0$ and $\mu_s = 0$ throughout the present study.

We take the temperature-dependent effective potential $\mathcal{U}(\Phi, \bar{\Phi}, T)$ from Ref. [21], i.e.,

$$\mathcal{U}(\Phi, \bar{\Phi}, T) = -b \cdot T\left\{54e^{-a/T}\Phi\bar{\Phi} + \ln\left[1 - 6\Phi\bar{\Phi} - 3\left(\Phi\bar{\Phi}\right)^2 + 4\left(\Phi^3 + \bar{\Phi}^3\right)\right]\right\}. \quad (7)$$

The parameters $a = 664$ MeV and $b = 0.028\Lambda^3$ are determined by the condition that the first-order phase transition in the pure gluodynamics takes place at $T = 270$ MeV[21], and the simultaneous crossover of the chiral restoration and the deconfinement phase transition occurs around $T \approx 212$ MeV. The Polyakov loop Φ and its (charge) conjugate $\bar{\Phi}$ are expressed as[48, 57]

$$\Phi = \frac{1}{N_c}\text{Tr}_c L, \qquad \bar{\Phi} = \frac{1}{N_c}\text{Tr}_c L^\dagger, \quad (8)$$

where $N_c = 3$ is the color degeneracy, and the matrix L in color space is explicitly given by

$$L(\boldsymbol{x}) = \mathcal{P}\exp\left[i\int_0^\beta d\tau A_4(\tau, \boldsymbol{x})\right] = \exp\left(\frac{iA_4}{T}\right), \quad (9)$$

with $\mathcal{P}$ being the path ordering and $\beta = 1/T$ being the inverse of temperature. The coupling between the Polyakov loop and quarks is uniquely determined by the covariant derivative D_μ in the pNJL Lagrangian [Eq. (1)][48]. The second equal sign in the above equation is valid by treating the temporal component of the Euclidean gauge field A_4 as a constant in the pNJL model. In this way, the Polyakov loop Φ and its conjugate $\bar{\Phi}$ can be treated as classical field variables.

Based on the mean-field approximation, the Lagrangian density of the pNJL model can be written as

$$\mathcal{L}_{\text{MF}} = \bar{\psi}S^{-1}\psi - \mathcal{V} - \mathcal{U}(\Phi, \bar{\Phi}, T), \quad (10)$$

where

$$S^{-1}(p) = \begin{pmatrix} S_{uu}^{-1}(p) & i\Delta\gamma^5 & 0 \\ i\Delta\gamma^5 & S_{dd}^{-1}(p) & 0 \\ 0 & 0 & S_{ss}^{-1}(p) \end{pmatrix} \quad (11)$$

is the inverse of the quark propagator $\mathcal{S}(p)$ as a function of quark momentum p, with

$$
\begin{aligned}
\mathcal{S}_{uu}^{-1}(p) &= \gamma^\mu p_\mu + \tilde{\mu}_u^\star \gamma^0 - M_u, \\
\mathcal{S}_{dd}^{-1}(p) &= \gamma^\mu p_\mu + \tilde{\mu}_d^\star \gamma^0 - M_d, \\
\mathcal{S}_{ss}^{-1}(p) &= \gamma^\mu p_\mu + \tilde{\mu}_s^\star \gamma^0 - M_s
\end{aligned}
$$

being the inverse of the u, d, and s quark propagators, respectively,

$$
\Delta = (G_S + 2G_{IS} - K\sigma_s)\pi \tag{12}
$$

being the gap parameter, and

$$
\begin{aligned}
\mathcal{V} &= G_S\left(\sigma_u^2 + \sigma_d^2 + \sigma_s^2\right) + \frac{G_S}{2}\pi^2 + G_{IS}(\sigma_u - \sigma_d)^2 + \\
&\quad G_{IS}\pi^2 - 4K\sigma_u\sigma_d\sigma_s - K\sigma_s\pi^2 - \\
&\quad \frac{1}{3}G_V(\rho_u + \rho_d + \rho_s)^2 - G_{IV}(\rho_u - \rho_d)^2
\end{aligned} \tag{13}
$$

being the condensation energy independent of the quark fields. In the above, $\rho_q = \langle \bar{q}\gamma^0 q \rangle$ and $\sigma_q = \langle \bar{q}q \rangle$ are the net-quark density and the chiral condensate, respectively, with $q = u, d, s$ being the quark flavor, and $\pi = \langle \bar{\psi}i\gamma^5\lambda^1\psi \rangle$ is the pion condensate. The constituent mass of quarks can be expressed as

$$
\begin{aligned}
M_u &= m_u - 2G_S\sigma_u - 2G_{IS}(\sigma_u - \sigma_d) + 2K\sigma_d\sigma_s, \\
M_d &= m_d - 2G_S\sigma_d + 2G_{IS}(\sigma_u - \sigma_d) + 2K\sigma_u\sigma_s, \\
M_s &= m_s - 2G_S\sigma_s + 2K\sigma_u\sigma_d + \frac{K}{2}\pi^2.
\end{aligned}
$$

The effective chemical potentials for u, d, and s quarks in the propagator are defined as

$$
\tilde{\mu}_u^\star = \frac{\tilde{\mu}_B}{3} - iA_4 + \frac{\tilde{\mu}_I}{2}, \tag{14}
$$

$$
\tilde{\mu}_d^\star = \frac{\tilde{\mu}_B}{3} - iA_4 - \frac{\tilde{\mu}_I}{2}, \tag{15}
$$

$$
\tilde{\mu}_s^\star = \frac{\tilde{\mu}_B}{3} - iA_4 - \tilde{\mu}_S, \tag{16}
$$

with the effective baryon, isospin, and strangeness chemical potentials expressed as

$$
\begin{aligned}
\tilde{\mu}_B &= \mu_B - 2G_V\rho, \\
\tilde{\mu}_I &= \mu_I - 4G_{IV}(\rho_u - \rho_d), \\
\tilde{\mu}_S &= \mu_S,
\end{aligned} \tag{17}
$$

and

$$
\begin{aligned}
\mu_B &= \frac{3(\mu_u + \mu_d)}{2}, \\
\mu_I &= \mu_u - \mu_d, \\
\mu_S &= \frac{\mu_u + \mu_d}{2} - \mu_s
\end{aligned} \tag{18}
$$

are the real baryon, isospin, and strangeness chemical potentials.

The thermodynamic potential of the quark system can be obtained through

$$
\Omega = -T\sum_n \int \frac{\mathrm{d}^3p}{(2\pi)^3}\,\mathrm{Tr}\ln\mathcal{S}(i\omega_n, \boldsymbol{p})^{-1} + \mathcal{V} + \mathcal{U}\left(\Phi, \bar{\Phi}, T\right). \tag{19}
$$

In the above, the four-momentum $p = (p_0, \boldsymbol{p})$ becomes $p = (i\omega_n, \boldsymbol{p})$ with $\omega_n = (2n+1)\pi T$ being the Matsubara frequency for a Fermi system. In order to evaluate Ω for each momentum p numerically, we need to find the zeros of $\mathcal{S}^{-1}(p)$. Similar to the method in Refs. [58−60], it can be proved that the eigenvalues λ_k $(k = 1, 2, 3, 4)$ of the following "Dirac Hamiltonian density"

$$
\mathcal{H}(\boldsymbol{p}) = -\begin{pmatrix}
\frac{\tilde{\mu}_I}{2} - M_u & |\boldsymbol{p}| & 0 & -\Delta \\
|\boldsymbol{p}| & \frac{\tilde{\mu}_I}{2} + M_u & \Delta & 0 \\
0 & \Delta & -\frac{\tilde{\mu}_I}{2} - M_d & |\boldsymbol{p}| \\
-\Delta & 0 & |\boldsymbol{p}| & -\frac{\tilde{\mu}_I}{2} + M_d
\end{pmatrix}
$$

are zeros of $\mathcal{S}^{-1}(p)$. Using the relationship $\mathrm{Tr}\ln = \ln\mathrm{Det}$, one can get the following expression of the thermodynamic potential

$$
\begin{aligned}
\Omega &= \Omega^+(\lambda_1') + \Omega^+(\lambda_2') + \Omega^-(-\lambda_3') + \Omega^-(-\lambda_4') + \\
&\quad \Omega^+(E_s^-) + \Omega^-(E_s^+) + \mathcal{V} + \mathcal{U}\left(\Phi, \bar{\Phi}, T\right)
\end{aligned} \tag{20}
$$

with

$$
\Omega^\pm(\lambda) = -2N_c\int_0^\Lambda \frac{\mathrm{d}^3p}{(2\pi)^3}\frac{\lambda}{2} - 2T\int_0^\Lambda \frac{\mathrm{d}^3p}{(2\pi)^3}Z^\pm(-\lambda), \tag{21}
$$

where the integrands in the second integral are

$$
\begin{aligned}
Z^-(\lambda) &= \mathrm{Tr}_c\ln(1 + L\xi_\lambda) = \ln\left\{1 + N_c\Phi\xi_\lambda + N_c\bar{\Phi}\xi_\lambda^2 + \xi_\lambda^3\right\}, \\
Z^+(\lambda) &= \mathrm{Tr}_c\ln(1 + L^\dagger\xi_\lambda) = \ln\left\{1 + N_c\bar{\Phi}\xi_\lambda + N_c\Phi\xi_\lambda^2 + \xi_\lambda^3\right\},
\end{aligned}
$$

with $\xi_\lambda = e^{\beta\lambda}$. In Eq. (20), λ_k' and $E_s^\pm$ are defined respectively as $\lambda_k' = \lambda_k - \frac{\tilde{\mu}_B}{3}$ and $E_s^\pm = E_s \pm \tilde{\mu}_s$, with $E_s = \sqrt{M_s^2 + \boldsymbol{p}^2}$ being the single s quark energy. Throughout this paper, Tr and Det represent respectively the trace and determinant over Dirac, flavor, and color space, while Tr_c and Det_c represent those only taken over color space. It should be pointed out that we introduce a momentum cutoff in the two integrals in Eq. (21) as in Ref. [51], otherwise the integrals will be divergent at large baryon and isospin chemical potentials. This is, however, slightly different from our previous studies[61−63].

By taking the trace of the corresponding component of the propagator[35], the chiral condensates σ_q, the net-quark densities ρ_q, and the pion condensate π can be expressed as

$$
\sigma_u = 4N_c\sum_{k=1}^4 \int \frac{\mathrm{d}^3p}{(2\pi)^3}g_{\sigma u}(\lambda_k)\left[-\frac{1}{2} + F^+(\lambda_k')\right], \tag{22}
$$

$$\sigma_d = 4 N_c \sum_{k=1}^{4} \int \frac{\mathrm{d}^3 p}{(2\pi)^3} g_{\sigma d}(\lambda_k) \left[-\frac{1}{2} + F^+(\lambda_k') \right], \qquad (23)$$

$$\sigma_s = 2 N_c \int \frac{\mathrm{d}^3 p}{(2\pi)^3} \frac{M_s}{E_s} [F^+(E_s^-) + F^-(E_s^+) - 1], \qquad (24)$$

$$\rho_u = 4 N_c \sum_{k=1}^{4} \int \frac{\mathrm{d}^3 p}{(2\pi)^3} g_{\rho u}(\lambda_k) \left[-\frac{1}{2} + F^+(\lambda_k') \right], \qquad (25)$$

$$\rho_d = 4 N_c \sum_{k=1}^{4} \int \frac{\mathrm{d}^3 p}{(2\pi)^3} g_{\rho d}(\lambda_k) \left[-\frac{1}{2} + F^+(\lambda_k') \right], \qquad (26)$$

$$\rho_s = 2 N_c \int \frac{\mathrm{d}^3 p}{(2\pi)^3} [F^+(E_s^-) - F^-(E_s^+)], \qquad (27)$$

$$\pi = 4 N_c \sum_{k=1}^{4} \int \frac{\mathrm{d}^3 p}{(2\pi)^3} g_{\pi}(\lambda_k) \left[-\frac{1}{2} + F^+(\lambda_k') \right], \qquad (28)$$

where the g functions have the same form as those in Ref. [31], since the g functions are actually independent of $\tilde{\mu}_B$, and the iA_4 terms are always combined with $\tilde{\mu}_B/3$ in the quark propagator. In the above, $F^+(\lambda)$ and $F^-(\lambda)$ are, respectively, the effective phase-space distribution for quarks and antiquarks, and they are expressed as

$$F^+(\lambda) = \frac{1}{N_c} \mathrm{Tr}_c \left(\frac{1}{1 + L\xi_\lambda} \right) = \frac{1 + 2\Phi\xi_\lambda + \bar{\Phi}\xi_\lambda^2}{1 + N_c\Phi\xi_\lambda + N_c\bar{\Phi}\xi_\lambda^2 + \xi_\lambda^3},$$

$$F^-(\lambda) = \frac{1}{N_c} \mathrm{Tr}_c \left(\frac{1}{1 + L^\dagger\xi_\lambda} \right) = \frac{1 + 2\bar{\Phi}\xi_\lambda + \Phi\xi_\lambda^2}{1 + N_c\bar{\Phi}\xi_\lambda + N_c\Phi\xi_\lambda^2 + \xi_\lambda^3}.$$

It is seen that the above distributions reduce to the normal Fermi-Dirac form at high temperatures when the Polyakov loops are approaching 1, while they become the Fermi-Dirac form with a reduced temperature of $T/3$ at low temperatures when the Polyakov loops are almost zero. This leads to a CEP at a higher temperature in the pNJL model than in the NJL model. Eqs. (22)~(28) can be also obtained equivalently from

$$\frac{\partial \Omega}{\partial \sigma_q} = \frac{\partial \Omega}{\partial \rho_q} = \frac{\partial \Omega}{\partial \pi} = 0, \qquad (29)$$

with $q = u, d, s$ being the quark flavor, leading to the relations

$$\sigma_q = \frac{\partial \Omega}{\partial M_q}, \quad \rho_q = -\frac{\partial \Omega}{\partial \mu_q}, \quad \pi = -\frac{\partial \Omega}{\partial \Delta}. \qquad (30)$$

The values of Φ and $\bar{\Phi}$ can be similarly determined by minimizing the grand potential with respect to the Polyakov loops, *i.e.*,

$$\frac{\partial \Omega}{\partial \Phi} = \frac{\partial \Omega}{\partial \bar{\Phi}} = 0. \qquad (31)$$

2 Results and discussions

With the theoretical framework described above, we will display how the order parameters, *i.e.*, the chiral condensate, the pion condensate, and the Polyakov loop, evolve with the baryon chemical potential, the isospin chemical potential, and the temperature. After discussing the interplay among these order parameters, we will then present the three-dimensional QCD phase diagram. Results in the present study based on the pNJL model will also be compared with those from the NJL model. In the NJL model with the same parameter values, the Polyakov-loop potential is turned off, and the covariant derivative D_μ is reduced to ∂_μ in Eq. (1).

2.1 Interplay among order parameters

We compare the pion and chiral condensates in baryon-rich quark matter at $T = 50$ and 100 MeV as a function of the isospin chemical potential based on the NJL and pNJL model in Fig. 1. One sees that the pion condensate appears around $\mu_I \sim m_\pi$ and disappears at very large μ_I or high temperatures. The appearance and disappearance of the pion condensate are second-order phase transitions at smaller μ_B. With the increasing μ_B, the disappearance of the pion condensate first becomes a first-order phase transition, and then the appearance of the pion condensate becomes a first-order one as well. At very large μ_B, there is no pion condensate. At intermediate μ_B, there exists a second nonzero solution π_2 (denoted as dashed lines), which corresponds to the local maximum of the thermodynamic potential and is called the Sarma phase[64] as detailed in Ref. [31]. It is seen that the pion superfluid phase (π) and the Sarma phase (π_2) exist in a broader region of chemical potentials and temperatures in the pNJL model than in the NJL model.

Figure 2 displays the temperature dependence of the pion and chiral condensates at various baryon and isospin chemical potentials. One sees that the difference in the behavior of the pion condensate between the pNJL model and the NJL model is mainly at high temperatures. The temperatures for the disappearance of pion condensates $\pi_{(2)}$ in the pNJL model are much higher than those in the NJL model, which will manifest themselves in the results of the phase diagrams to be shown later. Again, the pion superfluid phase (π) and the Sarma phase (π_2) exist in a broader region of temperatures in the pNJL model than in the NJL model.

Some common features in Figs. 1 and 2 need further discussions. According to the expressions of g functions in Ref. [31] and the gap equations [Eqs. (22)~(28)], both the chiral condensate and the net-quark densities depend on the gap parameter Δ or equivalently on the pion condensate $\pi_{(2)}$. Therefore, the sudden change of $\pi_{(2)}$, corresponding to
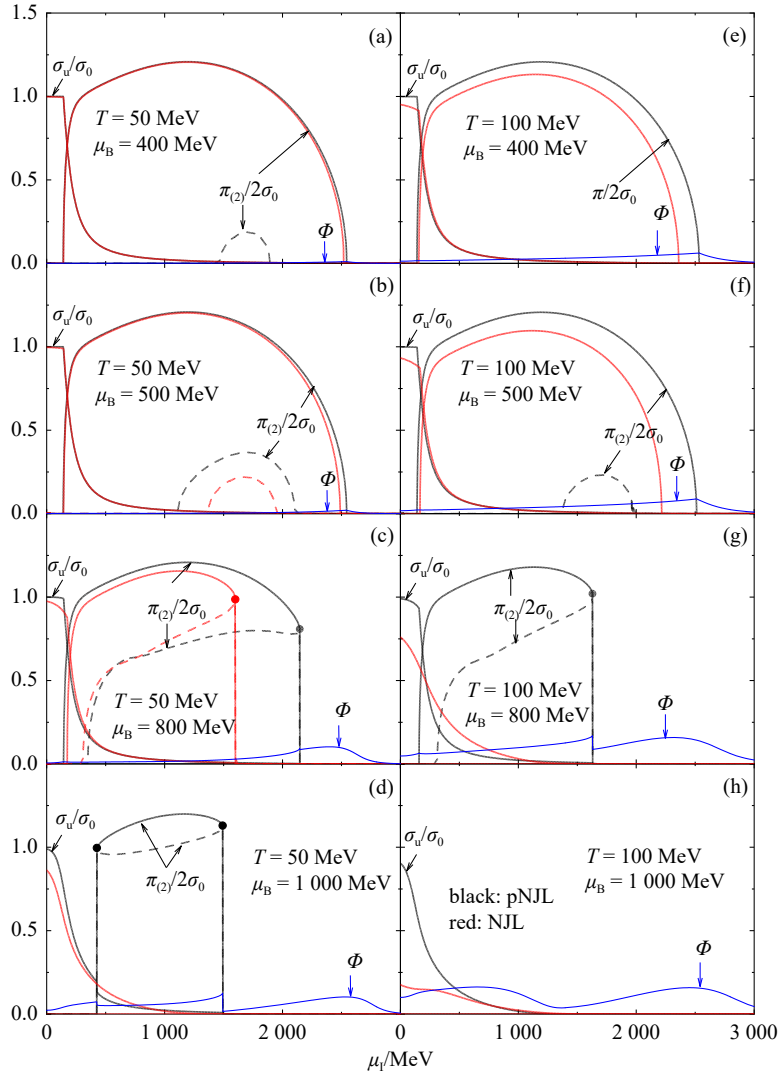
Fig. 1   Reduced pion condensate $\pi/2\sigma_0$, Sarma phase solution $\pi_2/2\sigma_0$, and chiral condensate σ_u/σ_0 as well as the Polyakov loop Φ as a function of the isospin chemical potential μ_I in hot [$T=50$ (left) and 100 (right) MeV] and baryon-rich [$\mu_B=400$ (a),(e), 500 (b),(f), 800 (c),(g), and 1000 (d),(h) MeV] quark matter. Results are compared with those obtained from the NJL model. (color online)
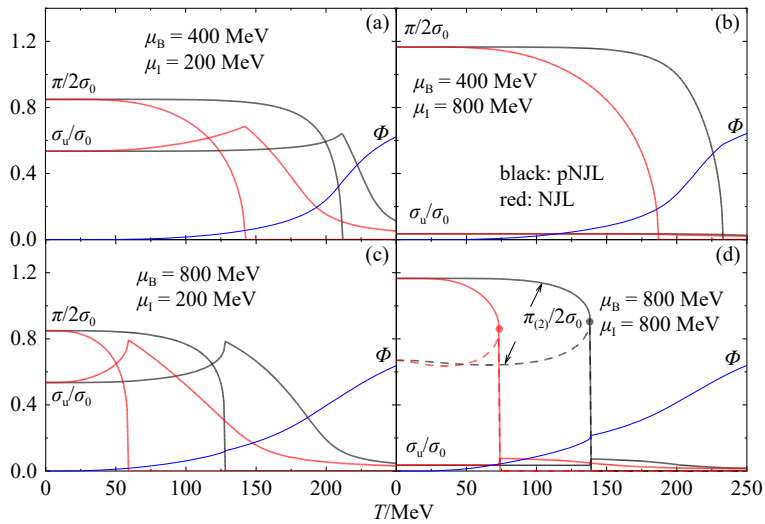

Fig. 2   Reduced pion condensate $\pi/2\sigma_0$, Sarma phase solution $\pi_2/2\sigma_0$, and chiral condensate σ_u/σ_0 as well as the Polyakov loop Φ as a function of the temperature T in quark matter of different baryon chemical potentials μ_B and isospin chemical potentials μ_I. Results are compared with those obtained from the NJL model. (color online)

either a first-order or a second-order phase transition of the whole quark matter system, leads to a sudden jump of the chiral condensates, the net-number densities as well as the Polyakov loop Φ. For the behavior of the Polyakov loop Φ, in principle one expects that it should increase with both the increasing chemical potential and temperature (see, *e.g.*, Fig. 10 in Ref. [21]), while the non-monotonical dependence of Φ on μ_I in Fig. 1 is due to the momentum cutoff in Eq. (21) when evaluating Eq. (31).

2.2 Three-dimensional QCD phase diagram

We now compare the three-dimensional (T, μ_B, μ_I) QCD phase diagram based on the pNJL model with that from the NJL model, and mainly focus on the phase structure relevant to the pion condensate. The resulting phase diagram will be shown in the $T-\mu_B$, $T-\mu_I$, and $\mu_B-\mu_I$ planes in Figs. 3, 4, and 5, respectively, where areas of the normal baryon-rich and isospin-asymmetric quark matter with $\pi = 0$ (Phases I), the pion superfluid phase with $\pi \neq 0$
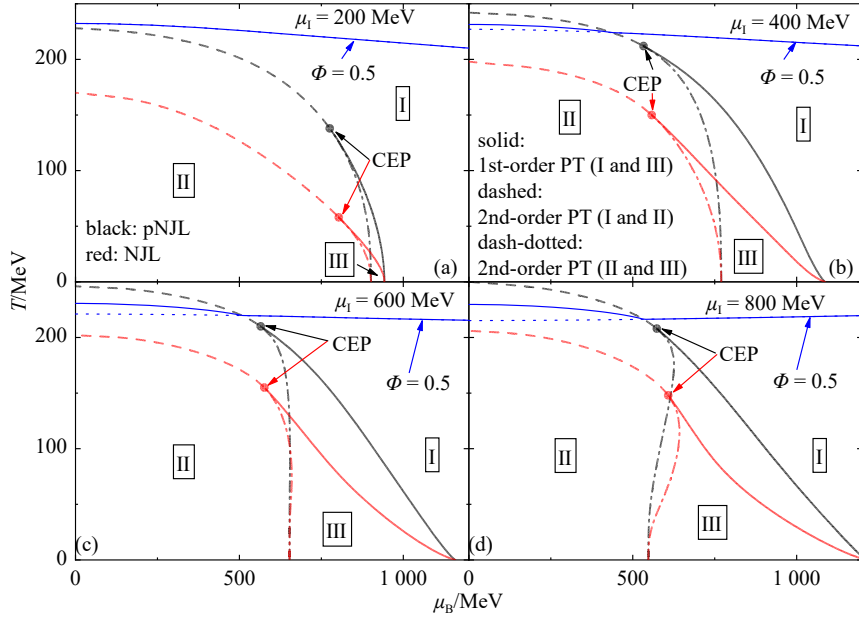

Fig. 3　Phase diagrams in the $T-\mu_B$ plane at different isospin chemical potentials $\mu_I = 200$ (a), 400 (b), 600 (c), and 800 (d) MeV in the pNJL model compared with those in NJL model. Solid lines represent the first-order phase transition (PT) between Phase I and Phase III, dashed lines represent the second-order phase transition between Phase I and Phase II, and dash-dotted lines represent the second-order phase transition between Phase II and Phase III. Blue solid (dotted) lines represent the deconfinement phase transition with (without) the pion condensate. (color online)
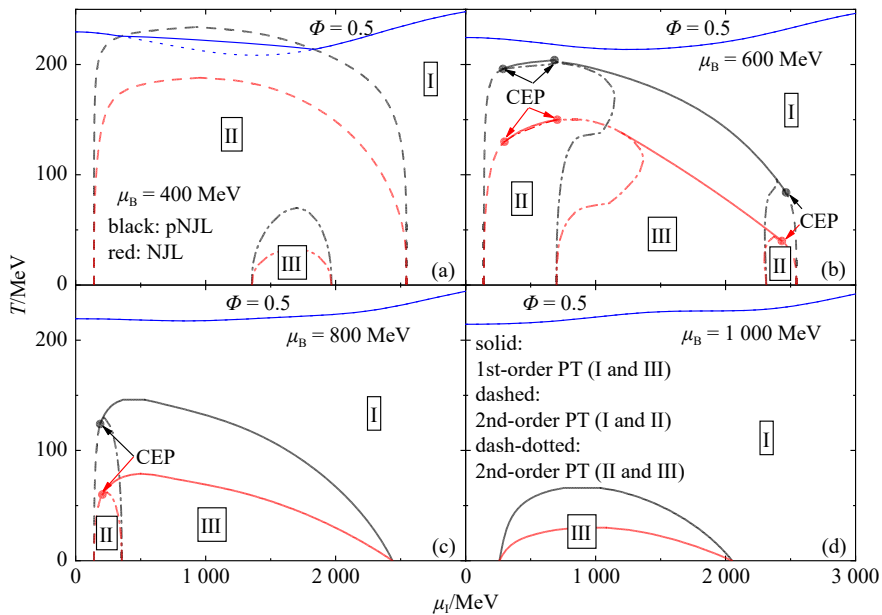

Fig. 4　Similar to Fig. 3 but in the $T-\mu_I$ plane at different baryon chemical potentials $\mu_B = 400$ (a), 600 (b), 800 (c), and 1 000 (d) MeV. (color online)
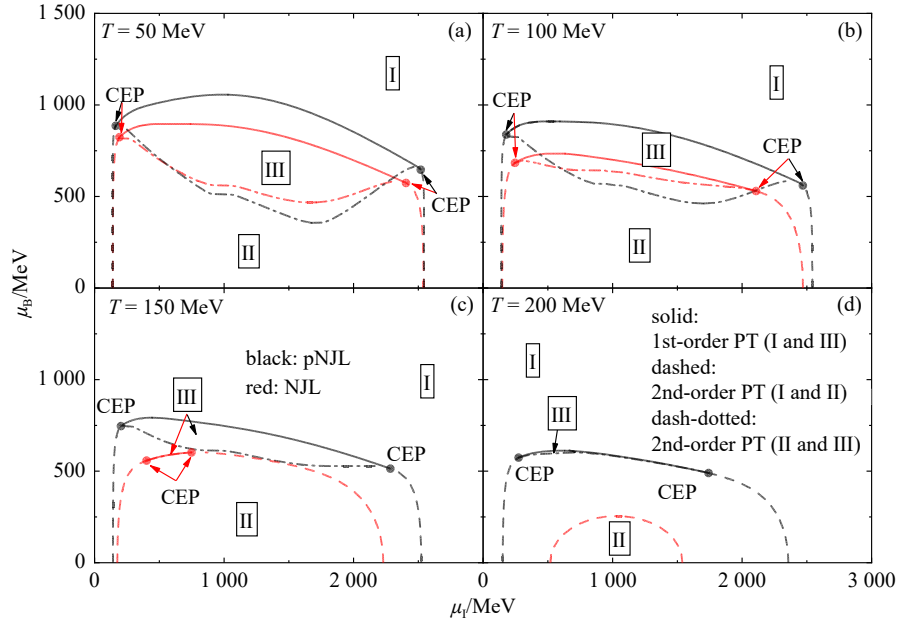
Fig. 5　Similar to Fig. 3 but in the $\mu_B - \mu_I$ plane at different temperatures $T =$ 50 (a), 100 (b), 150 (c), and 200 (d) MeV. (color online)

(Phase II), and the phase with both nonzero solutions of π and π_2 (Phase III) as well as the corresponding phase boundaries will be presented. The transitions between Phase I and Phase III are always a first-order one indicated by the solid line, while the transitions between Phase I and Phase II as well as those between Phase II and Phase III are always a second-order one indicated by the dashed lines and dash-dotted lines, respectively. The CEP is generally the crossing point for the three phases.

　　Figure 3 displays the phase diagrams in the $T - \mu_B$ plane at different isospin chemical potentials. For both NJL and pNJL models, Phase I generally exists at large T or large μ_B, while Phase II generally exists at small T and μ_B. The CEP connects the boundaries of the first-order phase transition and the second-order phase transitions, and it moves to a higher temperature when μ_I changes from 200 to 400 MeV, while the increasing trend becomes saturated above $\mu_I = 400$ MeV. Compared to the NJL model, the pN-JL model generally leads to larger areas of the pion superfluid phase and the Sarma phase, and a higher temperature of the CEP. Although the deconfinement phase transition in the pNJL model is always a smooth crossover, we plot an approximate deconfinement phase boundary obtained from $\Phi = 0.5$ with blue solid lines, and at smaller μ_B it moves slightly to lower temperatures if there is no pion condensate as shown by blue dotted lines.

　　Figure 4 displays the phase diagrams in the $T - \mu_I$ plane at different baryon chemical potentials. For both NJL and pNJL models, the normal quark phase (Phase I) is obtained at very small or large isospin chemical potentials, or at high temperatures. It is seen that the area of the pion superfluid phase (Phase II) becomes smaller with the increas-

ing baryon chemical potential. Second-order phase transitions are observed at small baryon chemical potentials, while first-order phase transitions occur at large baryon chemical potentials. Although not shown here, we find that Phase III with $\pi_2 \neq 0$ doesn't exist at $\mu_B = 0$, but it gradually appears inside Phase II at small baryon chemical potentials, and the area of Phase III generally increases with the increasing baryon chemical potential. Similar to that in the $T - \mu_B$ plane, the pNJL model leads to larger areas of the pion superfluid and Sarma phases and higher temperatures of the CEPs, compared to the NJL model. The deconfinement phase transition occurs at high temperatures, and is affected by the pion condensate at smaller μ_B and moderate μ_I.

　　Figure 5 displays the phase diagrams in the $\mu_B - \mu_I$ plane at different temperatures. For both NJL and pNJL models, the normal quark phase (Phase I) exists at larger μ_B and/or very small or large μ_I, and the pion superfluid phase (Phase II) is observed at smaller μ_B and moderate μ_I, already seen in Figs. 3 and 4. The area of Phase II becomes smaller with the increasing temperature. Also, the first-order phase transition and Phase III gradually disappear with the increasing temperature. Similarly, the pNJL model leads to larger areas of the pion superfluid and Sarma phases and CEPs at larger baryon chemical potentials, compared to the NJL model.

3　Summary and outlook

　　To summarize, by introducing the gauge field and the Polyakov effective potential into the Lagrangian density of the extended three-flavor NJL model, we have studied the

interplay among the chiral condensate, the pion condensate, and the Polyakov loop at finite temperatures, baryon chemical potentials, and isospin chemical potentials, and compared the three-dimensional QCD phase diagrams obtained from the NJL and pNJL models. While the two models give qualitatively similar QCD phase structures, we found that the pNJL model generally leads to larger areas of the pion superfluid phase and the Sarma phase, and the CEPs at higher temperatures. While the pion superfluid phase is stable, the Sarma phase corresponding to the local maximum of the thermodynamic potential is unstable against spatially inhomogeneous fluctuations, which can lead to the emergence of the Larkin-Ovchinnikov-Fudde-Ferrell phase[65] or other spatially separated phases. The present study, which includes effectively the gluon dynamics, provides a more reliable prediction of the three-dimensional QCD phase diagram compared to our previous study.

As is well-known, NJL-type models are not normalizable and a momentum cutoff is generally needed to avoid divergence in the integral. While the results, especially at large chemical potentials, do depend the regularization, the Pauli-Villars regularization scheme[66−67] could be a better choice compared to the sharp momentum cutoff, and can be investigated in future studies.

References:

[1] BERNARD C, BURCH T, GREGORY E B, et al. Phys Rev D, 2005, 71: 034504.

[2] AOKI Y, ENDRODI G, FODOR Z, et al. Nature, 2006, 443: 675.

[3] BAZAVOV A, BHATTACHARYA T, CHENG M, et al. Phys Rev D, 2012, 85: 054503.

[4] KARSCH F. Lect Notes Phys, 2002, 583: 209.

[5] MUROYA S, NAKAMURA A, NONAKA C, et al. Prog Theor Phys, 2003, 110: 615.

[6] BEDAQUE P F. EPJ Web Conf, 2018, 175: 01020.

[7] ADAMCZYK L, ADKINS J K, AGAKISHIEV G, et al. Phys Rev Lett, 2014, 112: 032302.

[8] ADAMCZYK L, ADKINS J K, AGAKISHIEV G, et al. Phys Rev C, 2017, 96(4): 044904.

[9] ODYNIEC G. PoS, 2013, CPOD2013: 043.

[10] WILCZEK F. Lect Notes Phys, 2011, 814: 1.

[11] ABLYAZIMOV T, ABUHOZA A, ADAK R P, et al. Eur Phys J A, 2017, 53(3): 60.

[12] AGAKISHIEV G, AGODI C, ALVAREZ-POL H, et al. Eur Phys J A, 2009, 41: 243.

[13] ABGRALL N, ANDREEVA O, ADUSZKIEWICZ A, et al. JINST, 2014, 9: P06005.

[14] ANTICIC T. PoS, 2009, EPS-HEP2009: 030.

[15] ANDRONOV E. Nucl Phys A, 2019, 982: 835.

[16] SORIN A, KEKELIDZE V, KOVALENKO A, et al. Nucl Phys A, 2011, 855: 510.

[17] SAKAGUCHI T. Nucl Phys A, 2017, 967: 896.

[18] YANG J C, XIA J W, XIAO G Q, et al. Nucl Instr and Meth B, 2013, 317: 263.

[19] BRATOVIC N M, HATSUDA T, WEISE W. Phys Lett B, 2013, 719: 131.

[20] ASAKAWA M, YAZAKI K. Nucl Phys A, 1989, 504: 668.

[21] FUKUSHIMA K. Phys Rev D, 2008, 77: 114028.

[22] CARIGNANO S, BUBALLA M. Phys Rev D, 2020, 101(1): 014026.

[23] XIN X Y, QIN S X, LIU Y X. Phys Rev D, 2014, 90(7): 076006.

[24] FISCHER C S, LUECKER J, WELZBACHER C A. Phys Rev D, 2014, 90(3): 034022.

[25] FU W J, PAWLOWSKI J M, RENNECKE F. Phys Rev D, 2020, 101(5): 054032.

[26] GAO F, PAWLOWSKI J M. Phys Rev D, 2020, 102(3): 034027.

[27] FRASCA M, RUGGIERI M. Phys Rev D, 2011, 83: 094024.

[28] HERBST T K, PAWLOWSKI J M, SCHAEFER B J. Phys Lett B, 2011, 696: 58.

[29] SCHAEFER B J, WAGNER M, WAMBACH J. Phys Rev D, 2010, 81: 074013.

[30] SON D T, STEPHANOV M A. Phys Rev Lett, 2001, 86: 592.

[31] LIU L M, XU J, PENG G X. Phys Rev D, 2021, 104(7): 076009.

[32] KLEIN B, TOUBLAN D, VERBAARSCHOT J J M. Phys Rev D, 2003, 68: 014009.

[33] BARDUCCI A, CASALBUONI R, PETTINI G, et al. Phys Rev D, 2004, 69: 096004.

[34] BARDUCCI A, CASALBUONI R, PETTINI G, et al. Phys Rev D, 2005, 72: 056002.

[35] HE L Y, JIN M, ZHUANG P F. Phys Rev D, 2005, 71: 116001.

[36] EBERT D, KLIMENKO K G. J Phys G, 2006, 32: 599.

[37] XIA T, HE L, ZHUANG P. Phys Rev D, 2013, 88(5): 056013.

[38] RÖβNER S, RATTI C, WEISE W. Phys Rev D, 2007, 75: 034007.

[39] ZHANG Z, LIU Y X. Phys Rev C, 2007, 75: 035201.

[40] ZHANG Z, LIU Y X. Phys Rev C, 2007, 75: 064910.

[41] SASAKI T, SAKAI Y, KOUNO H, et al. Phys Rev D, 2010, 82: 116004.

[42] MU C F, HE L Y, LIU Y X. Phys Rev D, 2010, 82: 056006.

[43] ADHIKARI P, ANDERSEN J O, KNESCHKE P. Phys Rev D, 2018, 98(7): 074016.

[44] LU Z Y, XIA C J, RUGGIERI M. Eur Phys J C, 2020, 80(1): 46.

[45] BRANDT B B, ENDRODI G, SCHMALZBAUER S. Phys Rev D, 2018, 97(5): 054514.

[46] KHUNJUA T, KLIMENKO K, ZHOKHOV R. Symmetry, 2019, 11(6): 778.

[47] FUKUSHIMA K. Phys Lett B, 2004, 591: 277.

[48] RATTI C, THALER M A, WEISE W. Phys Rev D, 2006, 73: 014019.

[49] FUKUSHIMA K, HATSUDA T. Rept Prog Phys, 2011, 74: 014001.

[50] FUKUSHIMA K, SKOKOV V. Prog Part Nucl Phys, 2017, 96: 154.

[51] COSTA P, RUIVO M C, DE SOUSA C A, et al. Phys Rev D, 2009, 79: 116003.

［52］ FU W J, ZHANG Z, LIU Y X. Phys Rev D, 2008, 77: 014006.

［53］ 'T HOOFT G. Phys Rev D, 1976, 14: 3432.

［54］ LUTZ M F M, KLIMT S, WEISE W. Nucl Phys A, 1992, 542: 521.

［55］ BUBALLA M. Phys Rept, 2005, 407: 205.

［56］ BRANDT B B, ENDRODI G, FRAGA E S, et al. Phys Rev D, 2018, 98(9): 094510.

［57］ PISARSKI R D. Phys Rev D, 2000, 62: 111501.

［58］ STEINER A W, REDDY S, PRAKASH M. Phys Rev D, 2002, 66: 094007.

［59］ FUKUSHIMA K, KOUVARIS C, RAJAGOPAL K. Phys Rev D, 2005, 71: 034002.

［60］ RUESTER S B, WERTH V, BUBALLA M, et al. Phys Rev D, 2005, 72: 034004.

［61］ LIU H, XU J, CHEN L W, et al. Phys Rev D, 2016, 94(6): 065032.

［62］ LIU L M, ZHOU W H, XU J, et al. Phys Lett B, 2021, 822: 136694.

［63］ ZHOU W H, LIU H, LI F, et al. Phys Rev C, 2021, 104: 044901.

［64］ SARMA G. Journal of Physics and Chemistry of Solids, 1963, 24: 1029.

［65］ HE L, JIN M, ZHUANG P. Phys Rev D, 2006, 74: 036005.

［66］ FLORKOWSKI W, FRIMAN B L. Z Phys A, 1994, 347: 271.

［67］ MU C, ZHUANG P. Eur Phys J C, 2008, 58: 271.

基于 pNJL 模型的三维 QCD 相图

刘鹿蒙[1], 徐 骏[2,3,4,†], 彭光雄[5]

(1. 中国科学院大学物理科学学院，北京 100049；

2. 同济大学物理科学与工程学院，上海 200092；

3. 中国科学院上海高等研究院，上海 201210；

4. 中国科学院上海应用物理研究所，上海 201800；

5. 中国科学院大学核科学与技术学院，北京 100049)

摘要： 基于三味 Polyakov-looped Nambu−Jona-Lasinio(pNJL) 模型，通过研究手征凝聚、pion 凝聚和 Polyakov 圈之间的相互作用，研究了温度、重子化学势和同位旋化学势依赖的三维 QCD 相图结构。虽然 pNJL 模型得到的正常夸克物质相、pion 超流相和 Sarma 相的结构以及相边界与 NJL 模型定性上相似，但 Polyakov 圈的引入大大扩展了 pion 超流相和 Sarma 相的存在区域，并导致临界点出现在较高的温度。由于有效地引入了胶子动力学的贡献，与 NJL 模型相比，该研究有望对三维 QCD 相图给出更可靠的预测。

关键词： NJL 模型；QCD 相图；pion 凝聚